Engineering Fracture Mechanics 246 (2021) 107626

Contents lists available at ScienceDirect

Engineering Fracture Mechanics

journal homepage: www.elsevier.com/locate/engfracmech

Observing progressive damage in carbon fiber epoxy laminate composites via 3D in-situ X-ray tomography

Alejandra M. Ortiz-Morales[1], Imad Hanhan[1], Jose Javier Solano[2], Michael D. Sangid *

School of Aeronautics and Astronautics, Purdue University, West Lafayette, IN, 47907, USA

ARTICLE INFO

Keywords:
(A) Polymer-matrix composites
(B) Micromechanics
(C) Crack growth
(D) Aerospace vehicles

ABSTRACT

As the use of fiber-reinforced polymer composites grows in aerospace structures, there is an emerging need to implement damage tolerant approaches. The use of *in-situ* synchrotron X-ray tomography enables direct observations of progressive damage relative to the microstructural features, which are studied in a T650/5320 laminate composite with two layups via monotonic tension. Specifically, the interactions of micromechanical damage mechanisms at the notch tip were analyzed through 3D image processing as the crack grew. The analysis showed intralaminar cracking was dominant during crack initiation, delamination became prevalent during the later stages of crack progression, and fiber breakage was, in general, largely related to intralaminar cracking.

1. Introduction

Polymer matrix composites have reshaped the aerospace industry, allowing engineers to reduce the overall weight of structures while retaining their required strength. To optimize performance, the mechanical behavior of fiber reinforced polymer matrix composites has been studied extensively, yet their mechanical response can be difficult to predict as they exhibit a number of damage mechanisms which can have complex interactions. These damage mechanisms have been categorized into three basic events which are typically observed in laminate composites: delamination, intralaminar cracking, and fiber breakage [1]. Delamination, which historically has been recognized as the most commonly observed damage mechanism in laminate composites, is defined as a discontinuity between two adjacent plies in a laminate composite [2–4]. On the other hand, intralaminar cracking represents a discontinuity that lies along the direction of the fibers and exists through the thickness of a ply [4,5]. Lastly, fiber breakage is a discontinuity in a fiber within the microstructure, which can sometimes occur in clusters of fibers [6,7].

Understanding the interaction of these mechanisms has been of interest for many decades, and much of it has been achieved through tailored experimental tests [8]. For instance, experiments utilizing circular holes in composite laminates through open hole tension tests are useful in understanding the damage behavior of composites assembled with fasteners [9]. Using classical lamination theory, Chang et al. produced one of the first progressive damage models for open hole laminate composites [10]. In their work, Chang et al. noted that initial failure of a $[(\pm 45)_6]_3$ composite with an open hole was in the form of fiber breakage, followed by damage along the fiber direction (intralaminar cracking) [10,11]. More recently, analyses of open hole tension tests have also included delamination as an active damage mechanism [9].

Yet, predicting the damage behavior of composites undergoing cyclic loading currently remains a major challenge. This is partly because many of the developed models lack flexibility when certain parameters (like the type of loading) are varied, resulting

* Corresponding author.
E-mail address: msangid@purdue.edu (M.D. Sangid).
[1] These authors contributed equally to writing this manuscript.
[2] Current affiliation: University of Houston, Houston, TX, 77004, USA.

https://doi.org/10.1016/j.engfracmech.2021.107626
Received 22 December 2020; Received in revised form 17 February 2021; Accepted 18 February 2021
Available online 24 February 2021

Nomenclature

μ-CT	Micro-computed tomography
μ_1, μ_2	Complex conjugate roots of characteristic equation with positive imaginary parts
ν_{12}	Poission's ratio
σ_Z	Stress in the Z direction
τ	Shear stress
θ	Angular coordinate from the crack tip
a_{ij}	Stiffness tensor
E_1	Young's modulus along fibers
E_2	Young's modulus normal to fibers
F_{ult}	Ultimate fracture force
G_{12}	Shear modulus
I	Intensity of a pixel
K_1	Mode I stress intensity factor
r	Radial distance from crack tip
DCB	Double cantilever beam
ROI	Region of interest

in significant differences in predicted behavior of the microstructure, especially immediately after damage initiation [12]. This trend can also be partially attributed to the difficulty researchers face in translating the results of a confined experimental test to a comprehensive predictive tool for composite structures. For example, double cantilever beam (DCB) experiments are commonly used to compute the mode I fracture toughness and examine the fatigue behavior of laminate composites [4]. While DCB tests provide an isolated focus on delamination that progresses perpendicular to the loading direction (which can sometimes be related to intralaminar fracture toughness), they often do not allow for the comprehensive constituent-level fracture behavior to be studied when delamination progresses parallel to the loading direction and simultaneously interacts with intralaminar cracking [4]. Therefore, with the safety of structures in mind, composite materials undergoing fatigue loading have been designed using a "no damage growth" philosophy, and their full potential has not yet been reached [13]. Specifically, this has resulted in composites being designed to operate below their fatigue endurance limit (with the aim of infinite life) and therefore have been generally over-designed [13,14]. While the present study focuses on monotonic loading, it offers a promising step towards understanding the damage behavior during cyclic loading, which will be further explored in future investigations.

More recently, there has been a larger focus on failure criteria at the constituent-level, for both experiments as well as simulations, in order to allow for more robust composite material application [15]. This is emphasized in the US Federal Aviation Administration Airworthiness Advisory Circular 20-107B, which calls for a slow damage growth philosophy to be applied to composites and adhesively-bonded joints [16,17]. Aligned with this approach, and with a focus on micromechanics, researchers have been working to comprehensively characterize the 3D microstructural damage behavior of laminate composites, and develop models that can aid in the prediction of damage tolerant behavior. As discussed in a recent review article by Garcea et al. [18], synchrotron-based X-ray micro-computed tomography (μ-CT) enables the opportunity to directly observe a 3D crack tip, and through time lapse CT (coupled with in-situ loading) the evolution of the crack tip can be studied. For laminate composites, μ-CT or related computed laminography has been used to characterize the damage events relative to the microstructural features, sometimes coupled with *in-situ* loading [7,19–24].

One such study, conducted by Wright et al. used *in-situ* μ-CT to examine damage growth in an edge notched $[90/+45/-45/0]_s$ carbon fiber epoxy composite specimen. They observed intralaminar cracking, delamination, and a relationship between fiber breakage and delamination at the $-45°/0°$ interface [25]. Interestingly, another study done by Scott et al. on a $[90/0]_s$ carbon fiber epoxy composite showed that there was no influence of matrix cracking on fiber breakage [26]. This reinforces that there can be significant layup dependencies on the microstructural damage initiation and propagation in composite materials.

In addition to damage being layup dependent, it has also been shown that the source of damage can affect the propagation of damage [1]. Therefore, there is a need to understand the initiation and propagation of damage using a fracture mechanics compact tension specimen design, which will allow for the simultaneous study of intralaminar cracking, delamination, and fiber breakage (including their interactions) in varying layup configurations [27,28]. To address this, the microstructural damage initiation and propagation of a carbon fiber epoxy composite with layups related to 45° has been analyzed in this work using compact tension specimens under monotonic tension, where damage grew from a sharp notch tip. Specifically, a T650/5320 composite was studied through *in-situ* X-ray μ-CT with layup configuration $[+45]_6$ (Specimen 1), which serves as a baseline for comparison, as well as a configuration of $[+45/-45/+45]_s$ (Specimen 2). This work used synchrotron X-rays in order to enable fast data acquisition which mitigates stress relaxation effects and enables continuous acquisition under increasing tension with minimum blur. The monotonic life of each specimen, with an emphasis on the quantification of the damage mechanisms (intralaminar cracking, delamination, and fiber breakage) and their interactions are shown. Overall, this work represents an important step towards understanding the micromechanical damage behavior of laminate composites under future fatigue loading, while providing a new case study of the 3D behavior of a composite microstructure in a compact tension specimen.

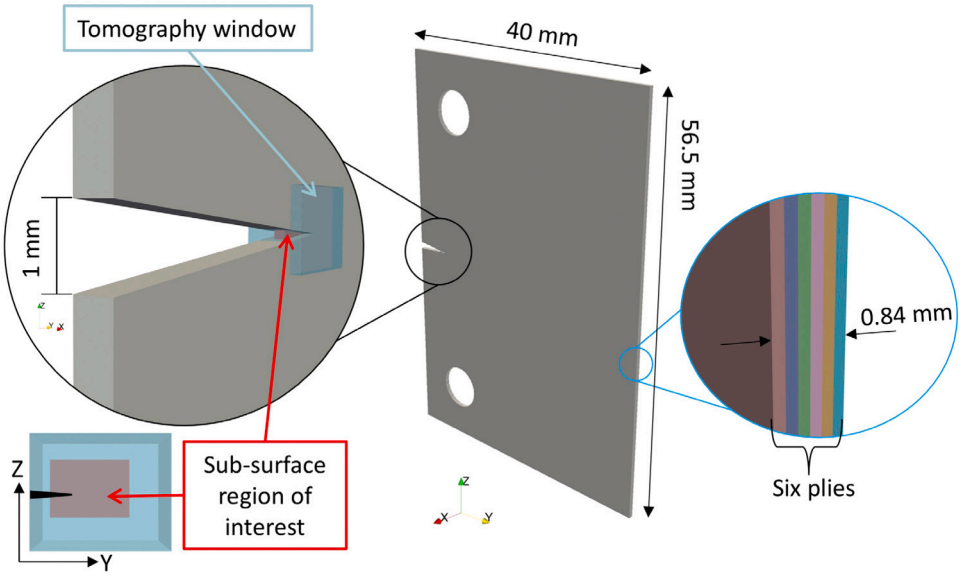

Fig. 1. The geometry of the compact tension specimens, where the left insert shows both the location of the tomography window at the sharp notch tip, as well as the sub-surface region of interest directly ahead of the sharp notch tip, and the right insert shows the thickness of the specimen which contained six plies.

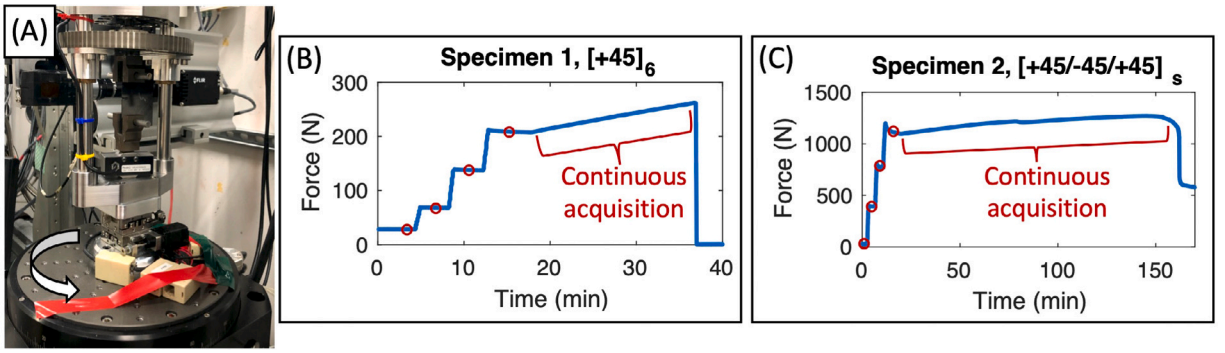

Fig. 2. An overview of the experiment, where (A) shows the *in-situ* tomography setup, custom miniature load frame, custom clevis grips, specimen held in compact tension, and rotational stage used to rotate the assembly during the acquisition of X-ray projections, (B) shows the load vs. time profile for Specimen 1 with layup $[+45]_6$, and (C) shows the load vs. time profile for Specimen 2 with layup $[+45/-45/+45]_s$. The incremental tomography acquisitions have been shown by red circles, and the continuous tomography acquisitions have been shown by red brackets.

2. Methodology

2.1. Materials

Carbon fiber epoxy laminate (T650/5320) panels were manufactured at the National Institute for Aviation Research at Wichita State University. The T650 carbon fibers have a tensile strength of 4.28 GPa and a fiber diameter of approximately 6.8 μm [29]. Two panels were used in this work, one with layup $[+45]_6$ and the other with layup $[+45/-45/+45]_s$. Prior to curing, isosceles triangular notches were cut (using an automated motorized razor) into the uncured prepreg at predetermined locations around the perimeter. Each triangular notch had a base dimension of 1 mm and a height of 5 mm, as shown in Fig. 1. The laminate panels were then cured in accordance to the manufacturer's specifications [30].

After curing, compact tension specimens were water-jet cut from the panels, maintaining the notch geometry in the midline of the specimen. The notches, which filled with resin during the cure cycle, were manually sharpened with a razor blade in order to remove the excess resin and create a sharp notch tip. While the geometry of the specimens was chosen to allow for a sharp notch akin to a classic compact tension specimen, it was also chosen to fit within the constraints of the custom miniature load frame, shown in Fig. 2A. These constraints included the height and width of the specimens as well as the position of the grips and the notch tip. Additionally, the notch tip had to be aligned with the center of rotation of the entire assembly to limit the procession of the specimen's region of interest during the image capture events of computed tomography. Due to these experimental constraints,

the specimens could not follow the compact tension ASTM geometric standards [31]. The specimen geometry can be seen in Fig. 1, where each specimen had a thickness of 0.84 mm, a width of 40 mm, and a height of 56.5 mm.

2.2. In-situ synchrotron X-ray tomography

The *in-situ* experiments were carried out at the Advanced Photon Source (beamline 2-BM) at Argonne National Laboratory using the tomography set-up shown in Fig. 2A. Shown on top of the rotational stage is the miniature load frame that used custom clevis grips to apply load on the compact tension specimens. The X-ray projections were captured with a pixel size of 0.69 μm. The beam energy was 25 keV and the sample to detector distance was 400 mm, with an exposure time per projection of 50 ms. The rotational stage, which held the load frame assembly, was rotated with a speed of approximately 2.5°/s over a total span of 180°, where an X-ray projection was acquired every 0.12°. Due to the load frame columns, 188 projections (of the total 1500) that were captured between 78° and 100.56° were not used for tomographic reconstruction.

Each specimen was monotonically loaded in tension using a custom screw-driven electromechanical load frame operated at a cross-head displacement of 0.002 mm/min. First, μ-CT images were acquired while the specimen was unloaded. Then, the specimen was loaded and held in tension by holding a constant cross-head displacement. After scanning at three incremental tension steps, continuous tensile loading was conducted at a cross-head displacement rate of 0.002 mm/min, and μ-CT images were continuously acquired. Specifically, the entire assembly was repeatedly rotated between 0° and 180°, and then back from 180° to 0°, while continuously acquiring X-ray projections, until the specimen fractured. Similarly to the static acquisition, projections captured between 78° and 100.56° were not used for tomographic reconstruction due to obstruction from the load frame's columns.

The force vs. time curves for Specimen 1 ($[+45]_6$) and Specimen 2 ($[+45/-45/+45]_s$) are shown in Fig. 2B and C, respectively. In the plots of Fig. 2, the incremental scans are circled in red and the continuous scanning is marked by a red bracket. Static displacement holds and μ-CT scans were conducted for Specimen 1 at the unloaded state, 68 N, 138 N, 210 N. The cross-head displacements corresponding to each of the static loading states for Specimen 1 were 0 mm, 0.034 mm, 0.087 mm, and 0.137 mm. After which continuous loading was conducted until fracture at a cross-head displacement of approximately 0.173 mm. Specimen 2 underwent a similar testing procedure, where static displacement holds and μ-CT scans were conducted at the unloaded state, 400 N, 800 N, and 1200 N. The cross-head displacements corresponding to each of the static loading states for Specimen 2 were 0 mm, 0.205 mm, 0.407 mm, and 0.647 mm. After which continuous loading was conducted until fracture at a cross-head displacement of approximately 0.851 mm. During the static cross-head displacement holds, both specimens were held for approximately 3.58 min, which resulted in an average force relaxation of 15.9 N.

Each tomography scan consisted of 1500 X-ray projections which were reconstructed using TomoPy [32]. The missing projections, which were caused by the load frame's columns, did not inhibit the quality of the reconstruction due to TomoPy's ability to handle missing projections [33]. The result was an image volume with dimensions 2048 by 2048 by 2046 voxels, with a voxel size of 0.69 by 0.69 by 0.69 μm. A schematic of the 3D grayscale image volume which is acquired via *in-situ* μ-CT (tomography window) is shown in the left insert of Fig. 1.

2.3. Matrix damage image processing

The tomography image stacks underwent several image processing techniques in order to detect the 3D matrix damage profile (intralaminar cracking or delamination) prior to the failure mode being assessed. First, the microstructure at each load increment, including the damage sustained, was visually inspected using the contrast enhancement tools in ImageJ [34]. A region of interest (ROI) was determined for each specimen based on two considerations. Firstly, the ROI was tailored to crop away locations behind the crack tip that were not of interest because they did not contain notable damage (which helped reduce the image processing computational costs). Secondly, based on observations of the 3D image volume captured just before fracture, the ROI was chosen to focus on areas with high concentrations of matrix cracking. The final ROI represented a critical location with complex damage interactions directly ahead of the crack tip, and it was tracked using 2D cross correlation throughout the loading history of each specimen. A schematic of the ROI within the full tomography window is also shown in the left insert of Fig. 1, where it can be seen that the ROI contains the very tip of the crack front.

After the ROI was determined at each load step, a set of algorithms were used to detect the voxels associated with matrix damage. The automated image processing, which was done using in-house Matlab algorithms, used parameters which varied depending on the specimen and the load step because the progression of damage created new internal surfaces, which caused new and increasing X-ray tomography artifacts. These varied parameters are represented as ranges $[min, max]$ in the following processing steps:

1. normalization of the grayscale intensity, I, so that $0 \leq I \leq 1$,
2. selection of voxels with $I < [0.5, 0.68]$,
3. removal of features with a volume smaller than $[30, 2000]$ voxels,
4. slice-by-slice 2D dilation using a disk structural element with radius $[5, 15]$ pixels,
5. dilation using a 3D spherical structural element with radius $[1, 4]$ voxels,
6. filling of volumes to remove internal holes
7. erosion using a 3D disk structural element with radius $[3, 12]$ voxels,
8. removal of features with a volume smaller than $[1000, 100\,000]$ voxels.

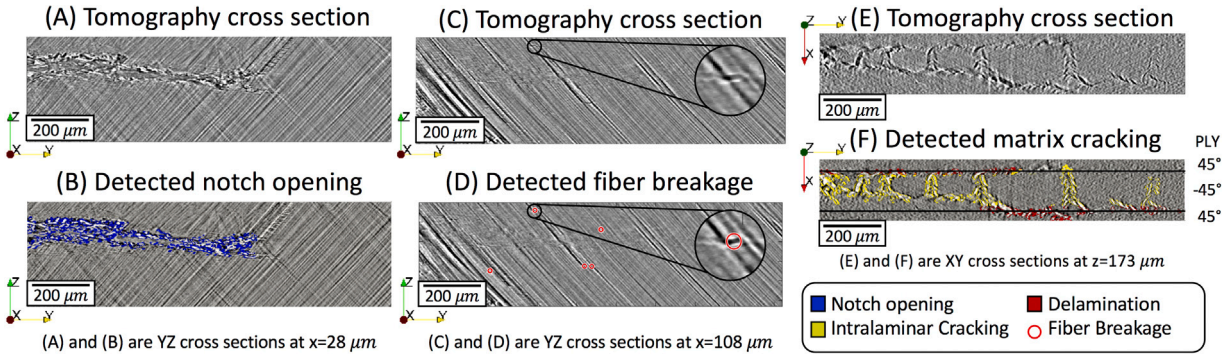

Fig. 3. Example of the validation of damage segmentation shown here for Specimen 2, with layup $[+45/-45/+45]_s$. The first row depicts tomography images, whereas the second row illustrates feature identification after image processing. Specifically, comparing tomography cross sections containing (A) the specimen notch with (B) the detected notch, (C) fiber breakage events with (D) the detected breakage and the sphere of influence, and (E) the matrix damage with (F) the classified matrix damage including intralaminar matrix cracking and delamination.

After each image processing step, ModLayer (a Matlab image processing graphical user interface) was used to validate the efficacy of matrix damage segmentation, and parameters were varied to ensure the highest accuracy in segmentation for each tomography scan [35]. This verification step was conducted for all load increments of both specimens, and a sample of this validation is shown in Fig. 3.

Using the open-source 3D visualization software ParaView [36], the matrix damage in each load step was manually categorized as either intralaminar cracking or delamination. Matrix damage was identified as intralaminar cracking if the damage was along the direction of the fibers and was generally through the thickness of a given ply. On the other hand, matrix damage was identified as delamination if the segmented region was located at a ply interface between two plies. An example of such a classification is shown in Fig. 3E and F. Lastly, the volume fraction of intralaminar cracking and delamination (compared to the total volume of matrix damage within the ROI) was computed at each load step to provide context into which mechanism was more active. During this manual characterization of damage, the notch tip within the ROI was also segmented (Fig. 3A and B) in order to contextualize the location of damage relative to the notch tip, as well as to differentiate it from the matrix damage.

2.4. Fiber breakage image processing

Fiber breakage in the tomography images was manually detected using ModLayer [35] for every load step of both specimens. The detection process consisted of analyzing each tomography slice in the YZ plane of the ROI. Side-by-side comparisons of a tomography slice at the unloaded state and a future load step (tracked using 2D image correlation) allowed for the observation of fiber breakage, as shown in Fig. 3C. Once a breakage event was observed, its center was located and the coordinates of this center were logged for further analysis.

In order to determine if there was an interaction between the matrix damage profile and the fiber breakage events, a sphere of influence criteria was established centered at each fiber breakage location where the sphere had a radius of 6.8 μm, approximately equivalent to one fiber diameter. A cross section of this sphere overlaid on a fiber breakage event is shown in Fig. 3D. Considering that there is some blur in the tomography images, a sphere of this size enabled the isolation and enclosure of the full breakage event as shown in the insert of Fig. 3D.

Each fiber breakage event was categorized as having some interaction with matrix damage using an automated Python shell in ParaView with the following implementation: a comparative analysis using the matrix damage detection procedure (discussed in Section 2.3) was performed to assess if the matrix damage profile intersected with the sphere of influence of each fiber breakage event. Specifically, each fiber breakage event was determined to have either no interaction, interaction with intralaminar cracking, or interaction with delamination depending on which damage events overlapped with each sphere of influence. After the interaction of each fiber breakage event was determined, the final visualizations representing the consolidation of the matrix cracking and fiber breakage data were done in ParaView to visualize the interaction of these damage micromechanisms.

2.5. Analytical computations

The stress fields ahead of the crack tip were assessed using a homogenized analytical solution to compare to the observed microstructural damage. For Specimen 1, the analytical solution represented the full ROI, which contained 2 plies oriented at 45°. For Specimen 2, the analytical solution was simplified to represent only the response in one ply within the ROI (which was oriented at −45°) in order to analyze the local response and not the full field response. The 2D analytical solution assumed several conditions, such as no pre-existing defects from manufacturing, and an idealized crack tip that is geometrically smooth, following the anisotropic elasticity equations developed by Sih et al. for crack-tip stresses in linearly anisotropic bodies [37]. For simplicity, the stress was divided by the mode I stress-intensity factor, K_I, to demonstrate trends and comparisons for the two specimens (in which K_I is

different and evolving with loading). The stress field, σ_Z, in the small region ahead of the crack tip was determined for in-plane symmetric loading of the composite laminate (corresponding to the loading direction in this work, Z) by

$$\frac{\sigma_Z}{K_I} = \frac{1}{\sqrt{2r}} Re\left[\frac{1}{\mu_1 - \mu_2}\left(\frac{\mu_1}{\sqrt{\cos\theta + \mu_2 \sin\theta}} - \frac{\mu_2}{\sqrt{\cos\theta + \mu_1 \sin\theta}}\right)\right] \tag{1}$$

and the shear stress, τ, was computed by

$$\frac{\tau}{K_I} = \frac{1}{\sqrt{2r}} Re\left[\frac{\mu_1\mu_2}{\mu_1 - \mu_2}\left(\frac{1}{\sqrt{\cos\theta + \mu_1 \sin\theta}} - \frac{1}{\sqrt{\cos\theta + \mu_2 \sin\theta}}\right)\right] \tag{2}$$

where r is the radial distance from the crack tip, θ is the angular coordinate from the crack tip, and Re represents the real part of a number. Here, μ_1 and μ_2 are determined from the two conjugate complex roots from the following characteristic equation:

$$a_{11}\mu^4 - 2a_{16}\mu^3 + (2a_{12} + a_{66})\mu^2 - 2a_{26}\mu + a_{22} = 0 \tag{3}$$

The stiffness tensor, a_{ij}, was constructed given the elastic constants of a unidirectional 0° lamina of T650/5320 [30], where E_1 is 138.4 GPa, E_2 is 9.175 GPa, G_{12} is 4.949 GPa, and υ_{12} is 0.326. Given the stiffness matrix for the unidirectional lamina with vertically aligned fibers, a stiffness matrix was calculated representing a fiber orientation of 45° for the analysis of two 45° plies in the ROI of Specimen 1, and of −45° for the analysis of one −45° ply in the ROI of Specimen 2. While this neglected the effects of the surrounding plies that face opposite directions in Specimen 2, it allowed for a comparison of the characterized damage in the local ply to the stress response in the local ply (as opposed to the bulk stress response of all the plies).

Due to the 3D nature of the tomography scans, a projection of the experimental damage was essential to enable its juxtaposition with the 2D analytical solution. This projection was achieved by consolidating the 3D damage data at the locations matching the analytical solution onto a 2D plane through several steps. An automated algorithm, written in Matlab, was used to create a 2D projection of the notch tip and the profile of matrix cracking. This was accomplished by summing the binarized matrix damage in each YZ plane within the ply or plies of interest, resulting in a damage depth metric (a 2D projection of the 3D damage). For Specimen 1, this was done for the full ROI which contained 286 YZ slices. For Specimen 2, this was done for only one ply within the ROI (which was oriented at −45°) and contained 210 YZ slices. Finally, the position of each fiber breakage event was superimposed to spatially correlate the breakage events and the distribution of the analytical stresses ahead of the crack tip.

3. Results

Specimen 1, with layup $[+45]_6$, failed at approximately 259 N as can be seen in Fig. 2B, where brittle fracture was observed to occur at the notch tip. Specimen 2, with layup $[+45/-45/+45]_s$, experienced a ductile fracture as can be seen in Fig. 2C. For Specimen 2, eventual fracture was not catastrophic, and the specimen did not completely fail. Instead, after the load significantly dropped, the damage at the crack tip grew outside the boundary of the tomography window (1689 by 1689 by 1411 μm), and there was significant damage at the pin attachment of the top clevis grip. For the purpose of comparing the results, the point at which the load significantly dropped for Specimen 2 will be considered the fracture point, which occurred at approximately 1263 N.

The progression of damage was tracked for both specimens, where the notch tip, matrix cracking, and fiber breakage events were identified in the ROI at each increment of load. In the unloaded state for Specimen 1 and Specimen 2, the volume of the notch tip comprised 0.2% and 0.3% of the ROI, respectively. Just before fracture, the volume of the notch tip and the newly formed damage in the microstructure comprised 0.6% and 4.3% of the ROI, in Specimen 1 and 2, respectively. This shows that the 3D crack was observed to grow significantly in the more ductile Specimen 2 leading up to fracture.

3.1. Damage in Specimen 1 with layup $[+45]_6$

The notch tip within the ROI for Specimen 1 is shown in Fig. 4A and B. In the first three static load increments of Specimen 1 captured at 68 N, 138 N, and 210 N, no damage was detected. Damage initiation was detected during continuous monotonic loading, at the scan captured at approximately 234 N ($0.9F_{ult}$). Specifically, matrix damage in the form of intralaminar matrix cracking was observed with a length of 111 μm, as shown in Fig. 4C. At the very end of continuous loading and tomography scanning (just before fracture at approximately 259 N), it was observed that the intralaminar matrix crack grew to a length of 209 μm, as shown in Fig. 4D. None of the captured tomography scans for this specimen showed any signs of delamination. After the last captured scan, damage progressed almost instantaneously and brittle fracture occurred. Fiber breakage events only occurred just before fracture in 19 locations, shown in Fig. 5. Among these locations, only one fiber breakage event interacted with intralaminar cracking, shown as a yellow sphere in Fig. 5.

3.2. Damage in Specimen 2 with layup $[+45/-45/+45]_s$

The notch tip within the ROI for Specimen 2 is shown in Fig. 6A and B. Damage initiation was observed in the first static load increment of Specimen 2, which was captured at 400 N ($0.3F_{ult}$). Specifically, matrix damage in the form of intralaminar cracking was observed, shown in Fig. 6C. In the second static load increment captured at 800 N ($0.6F_{ult}$), new locations of intralaminar cracking were detected, and the first signs of delamination appeared, but were minimal (Fig. 6D and H).

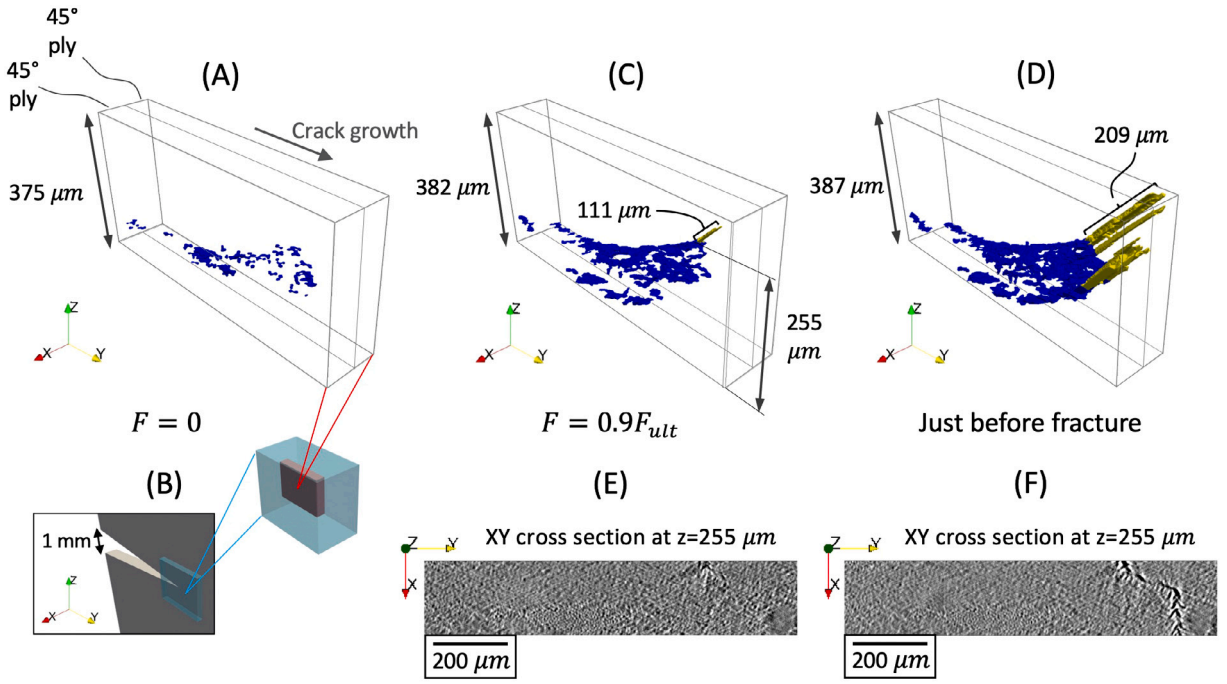

Fig. 4. Matrix cracking (which progresses from left to right) in Specimen 1, with layup $[+45]_6$, (A) at 0 N, where a schematic of the notch highlighting the ROI is shown in (B), (C) at 234 N ($0.9F_{ult}$), and (D) at 259 N ($0.99F_{ult}$), where only intralaminar cracking was observed emanating from the notch tip. In the 3D visualizations of damage, blue represents the notch tip and yellow represents intralaminar cracking. Tomography XY cross sections, with plane normal (along the Z direction) parallel to the loading direction, at $z = 255$ μm are shown (E) at 234 N, and (F) at 259 N where the evolution of damage is observed as load increases.

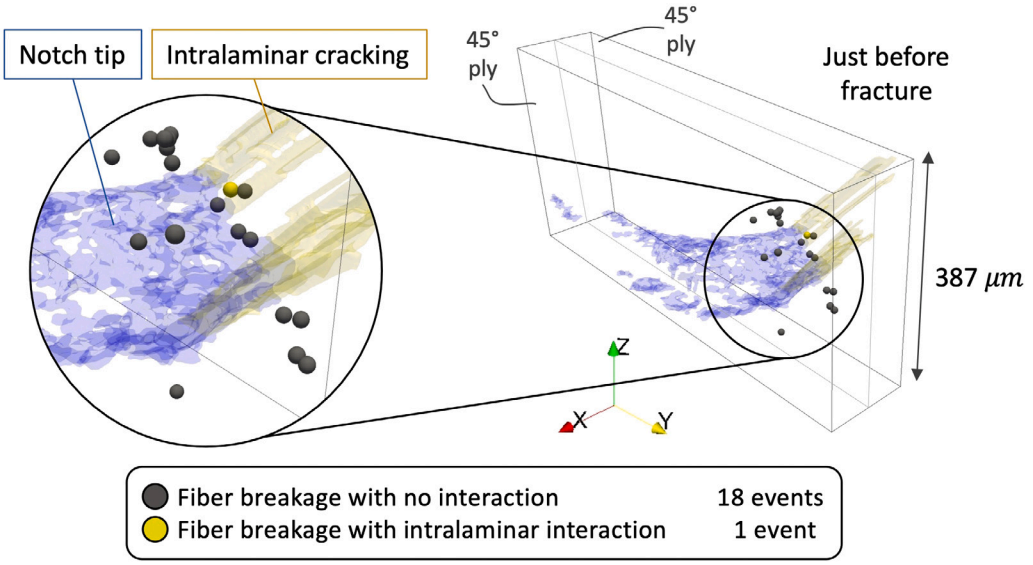

Fig. 5. Fiber breakage in Specimen 1, with layup $[+45]_6$, at the tomography image captured just before fracture (the only tomography scan which contained fiber breakage).

At the third static load increment, captured at 1200 N ($0.95F_{ult}$), intralaminar cracking continued to grow and represented 82.5% of the matrix damage profile (by volume). Additionally, the location of delamination grew, a new location of delamination was detected, and delamination represented 17.5% (by volume) of the matrix damage profile (Fig. 6E). Finally, at the last scan captured (which was taken just before fracture at the end of continuous loading), intralaminar cracking and delamination had

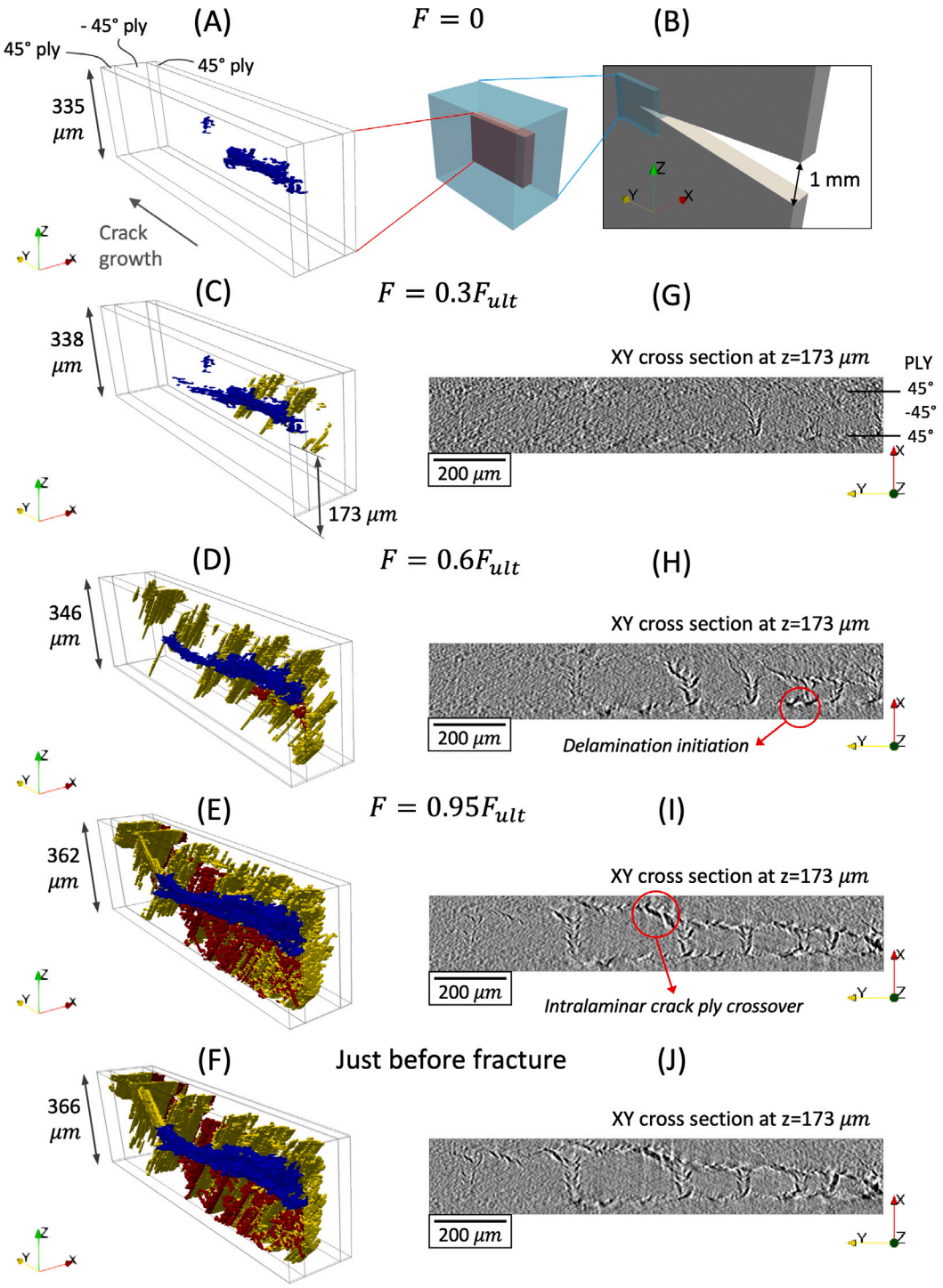

Fig. 6. Matrix cracking (which progresses from right to left) in Specimen 2, with layup $[+45/-45/+45]_s$ (and with black outlines showing the plies in the ROI), (A) at 0 N, where a schematic of the notch is shown in (B), (C) at 400 N ($0.3F_{ult}$), (D) at 800 N ($0.6F_{ult}$), (E) at 1200 N ($0.95F_{ult}$), and (F) just before fracture, where the volume fraction of each matrix cracking mechanism has been quantified at each load step. In the 3D visualizations of damage, blue represents the notch tip, yellow represents intralaminar cracking, and red represents delamination. Tomography XY cross sections, with plane normal (along the Z direction) parallel to the loading direction, at $z = 173$ μm are shown (G) at 400 N, (H) at 800 N, (I) at 1200 N, and (J) just before fracture, where the evolution of damage is observed with increasing load. In particular, sites of (H) delamination initiation are observed, as well as (J) sites where intralaminar cracks cross into neighboring plies.

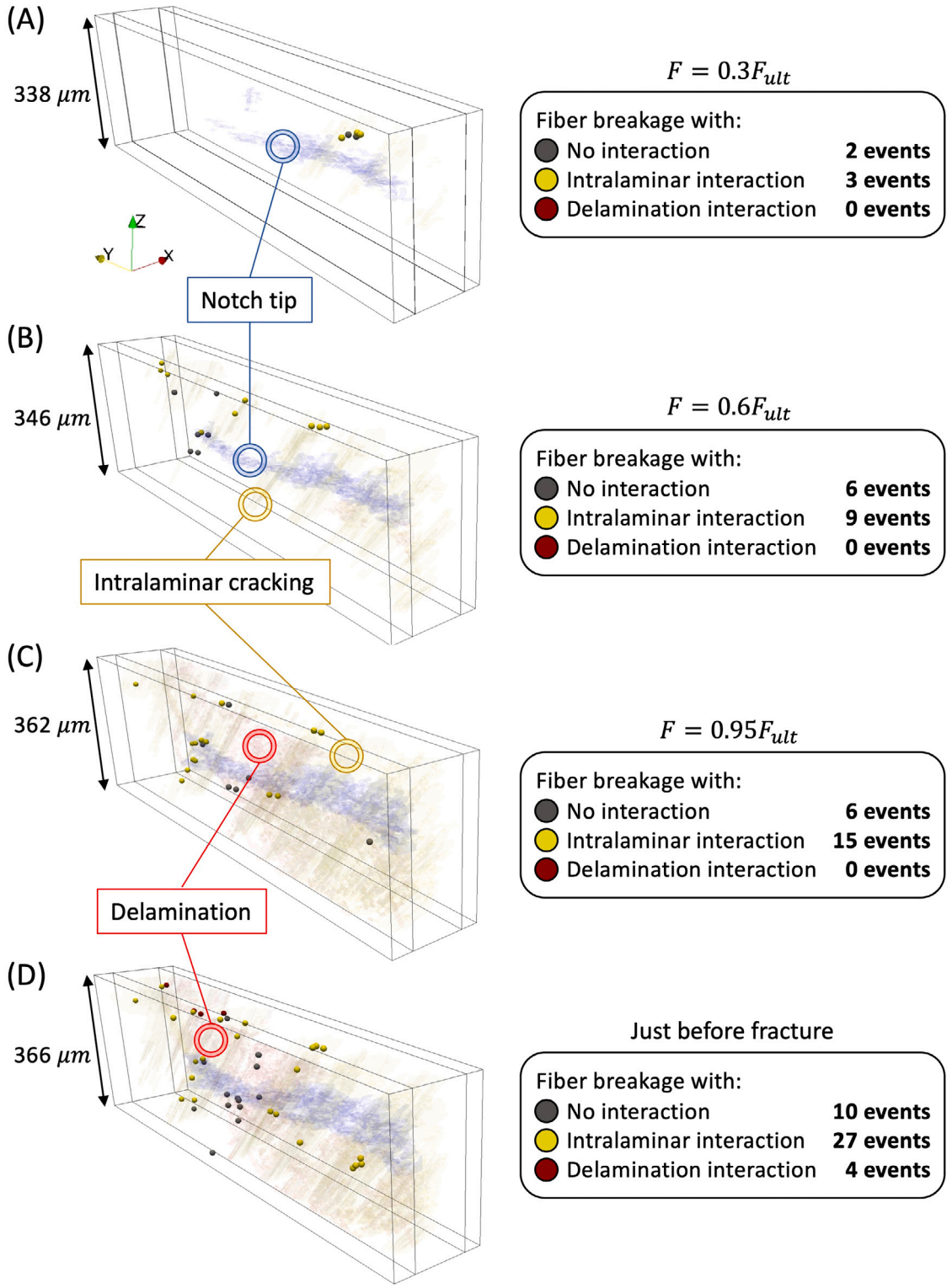

Fig. 7. Fiber breakage in Specimen 2, with layup $[+45/-45/+45]_s$ (with black outlines showing the plies in the ROI), at (A) 400 N ($0.3F_{ult}$), (B) 800 N ($0.6F_{ult}$), (C) 1200 N ($0.95F_{ult}$), and (D) just before fracture, where it can be seen that fiber breakage has a more prevalent interaction with matrix cracking, including delamination. The fiber breakage events shown here are new fiber breaks at each load state (not cumulative).

grown steadily, where intralaminar cracking remained the dominant matrix damage mechanism near the notch tip, as can be seen in Fig. 6F.

Fiber breakage was detected at the first load increment captured at 400 N ($0.3F_{ult}$), with a total of 5 fiber breakage events. Three of these events interacted with locations of intralaminar cracking, shown by the yellow spheres in Fig. 7A. Then, at 800 N, there were 15 new locations of fiber breakage, where 6 of these interacted with intralaminar cracking (Fig. 7B). Further, at 1200 N, 21 new locations of fiber breakage were detected, where 15 interacted with intralaminar cracking (Fig. 7C). Finally, just before fracture, there were 41 new events of fiber breakage, and the first interaction between fiber breakage and delamination was documented. Here, 27 fiber breakage events interacted with intralaminar cracking, and 4 breakage events were observed to interact with delamination at the ply interfaces (red spheres in Fig. 7D). Cumulatively, by the end of the loading sequence and just before fracture, Specimen 2 contained 82 total locations of fiber breakage events in the ROI: 24 were isolated from matrix damage and exhibited no interaction, 54 interacted with intralaminar cracking, and 4 interacted with delamination.

4. Discussion

Macroscopically, the observed behavior was very different between the two specimens analyzed in this study. Compared to compact tension Specimen 1 ($[+45]_6$), the alternating ply orientation in compact tension Specimen 2 ($[+45/-45/+45]_s$) resulted in a strength that was nearly five times higher, and, as expected, showed a higher degree of ductility. Microscopically in the epoxy matrix, both specimens showed signs of intralaminar cracking in the vicinity of the notch tip during damage initiation. However, during damage propagation, Specimen 1 ($[+45]_6$) showed progression in matrix damage that was exclusively in the form of intralaminar cracking along the direction of the fibers. This exclusive intralaminar cracking in the matrix grew quickly at the end of the monotonic life of the specimen when brittle fracture occurred.

On the other hand, Specimen 2 (with layup configuration $[+45/-45/+45]_s$) showed matrix damage propagation that was a combination of intralaminar cracking and delamination. This combined behavior appeared in the second half of the monotonic loading sequence, where it was shown that the first signs of delamination appeared at $0.6F_{ult}$, circled in Fig. 6H. This delamination behavior likely provided stress relief to the microstructure. Towards the end of the loading sequence (at $0.95F_{ult}$), delamination appeared to provide a path for the intralaminar crack to transition to a neighboring ply oriented in the opposite direction, as can be seen in Fig. 6I. Delamination, and its role in transitioning intralaminar cracks to neighboring plies, provided the increased macroscopic ductility observed in this specimen. Despite the important role of delamination in the ductile behavior shown in Specimen 2, it only comprised 20% of the matrix damage profile compared to intralaminar cracking in the ROI, as was shown in Fig. 6F.

As for fiber breakage, Specimen 1 ($[+45]_6$) contained fiber breakage events that were spatially located near the crack tip, however they showed almost no overlap with the locations of matrix damage. This can be seen in Fig. 5, where only 1 of 19 fiber breakage events interacted with intralaminar matrix cracking. In contrast, Specimen 2 ($[+45/-45/+45]_s$) showed the first signs of fiber breakage during damage initiation as can be seen in Fig. 7A. As matrix damage continued to progress with increased loading, new locations of fiber breakage events were observed, as shown in Fig. 7B–D. This relationship is likely the result of intralaminar cracking occurring first (since the epoxy matrix has a lower strength), which causes some of the neighboring carbon fibers to withstand higher local stresses and therefore experience breakage. Overall in Specimen 2, there was an observed correlation between fiber breakage and intralaminar cracking, where 54 out of the total 82 fiber breakage events interacted with intralaminar cracking. On the other hand, there was not a strong observed correlation between fiber breakage and delamination, where only 4 of the total 82 fiber breakage events interacted with intralaminar cracking.

The relationship between fiber breakage and intralaminar cracking observed in this work for a $[+45/-45/+45]_s$ layup can be contrasted to the behavior that has been observed for a $[90/0]_s$ carbon fiber epoxy layup, where Scott et al. showed that fiber breakage had no relationship with intralaminar cracking in that layup [26]. On the other hand, when analyzing a $[90/+45/-45/0]_s$ carbon fiber epoxy layup, Wright et al. found that there was a relationship between intralaminar cracking in the 45° ply and fiber breakage in the 0° ply as the intralaminar crack transitioned to the 0° ply [25]. This implies that the redistribution of stress provided by a 45° ply may play a crucial role in fiber breakage behavior.

Additionally in Specimen 2, a location of fiber bridging was directly observed, and has been visualized in Fig. 8. A simple location of delamination is shown in Fig. 8D, and can be compared to the location of fiber bridging in Fig. 8E. This observation shows that fiber bridging is a phenomenon which occurs in configurations other than a DCB test (such as the compact tension configuration in this work). Specifically, fiber bridging can be an active mechanism that increases fracture toughness and resists slow crack growth in composites [38] even when the plane of delamination (YZ plane) is aligned with the loading direction (Z direction). It was unexpected that the fibers which bridge the delamination gap were still intact and did not break, considering that bridging fibers produce high closure over a small displacement while experiencing high stress, sometimes leading to fiber breakage [39,40]. This implies that the relationship between delamination, fiber bridging, and fiber breakage is more complex than previously hypothesized, and may be heavily dependent on microstructural defects near the ply interface [38].

To examine the nature of matrix cracking and fiber breakage events, the analytical stress solution, shown in Fig. 9A, B, D, and E, which was computed in the vicinity of the crack tip within each specimen's ROI, sheds some light on the micromechanical behavior for each specimen. The experimental behavior can be compared in Fig. 9C and F, where the crack tip before damage initiation is outlined in red, the crack just before fracture is outlined in white, and red circles show the 2D projected locations of fiber breakage. As can be seen in Fig. 9A and B, the stress field in the homogenized ROI for Specimen 1 follows the direction of the fibers, where the highest shear stress occurs directly below and to the left of the notch tip (Fig. 9B) at the smaller angle between the fiber direction

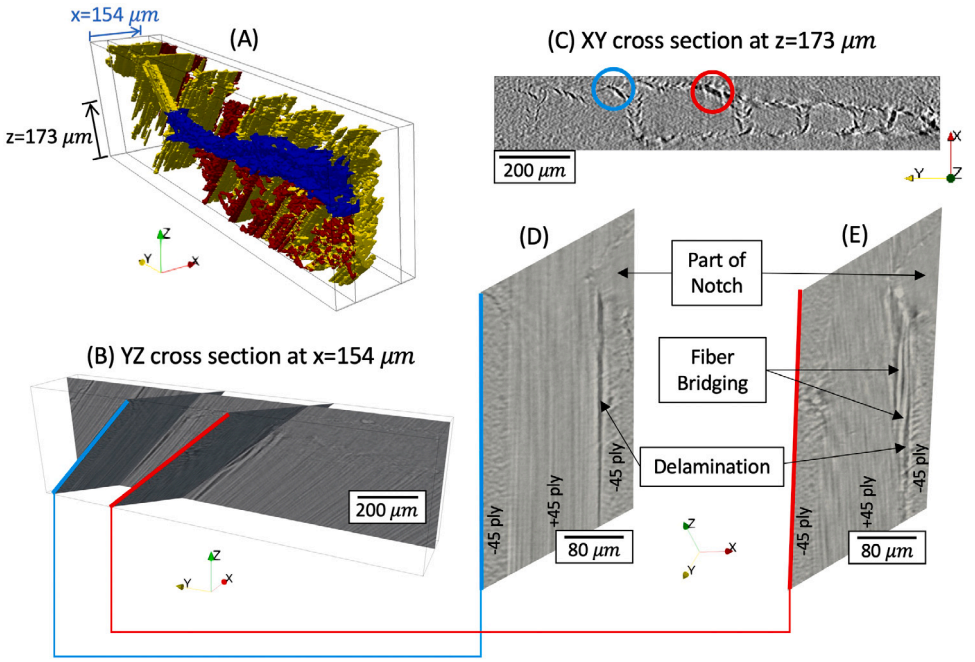

Fig. 8. The 3D matrix cracking detection is shown in (A) for reference, where a YZ cross section at $x = 154$ μm is shown in (B) that intersects two locations of delamination which have also been circled in (C) at an XY cross section at $z = 173$ μm. The first example of delamination is a typical delamination event and is shown in (D), and the second example contains fiber bridging and is shown in (E). Note that the two oblique cross sections in (D) and (E) were not parallel in order to clearly show the bridging fibers in (E).

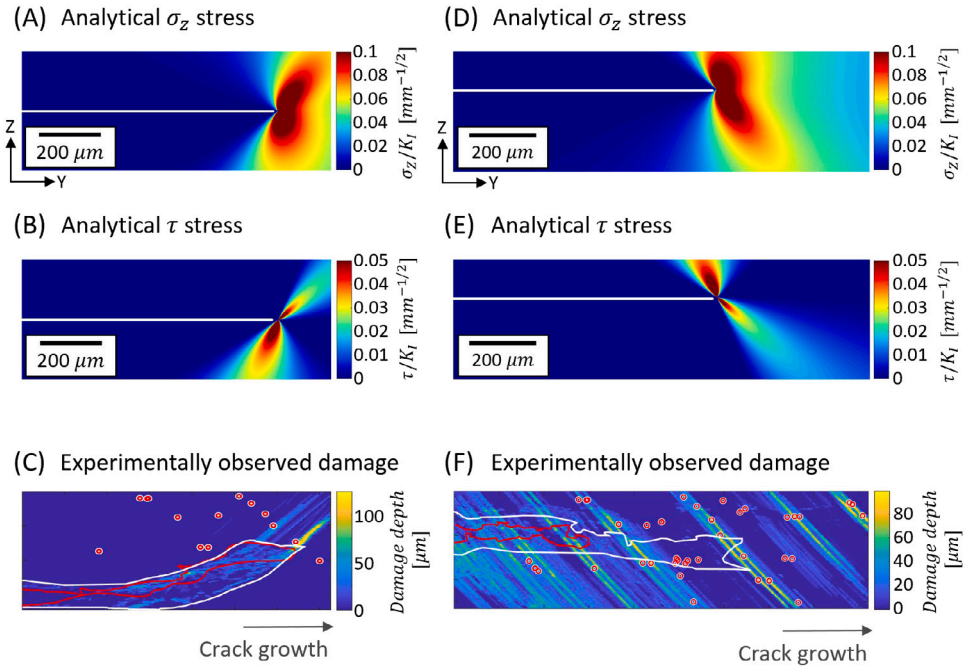

Fig. 9. Crack tip stress fields for Specimen 1, with layup $[+45]_6$, and Specimen 2, with layup $[+45/-45/+45]_s$. The σ_Z stress shown was determined (A) for Specimen 1 and (D) for Specimen 2, as well as the τ stress components calculated (B) for Specimen 1 and (E) for Specimen 2. The experimentally observed damage shown (C) for Specimen 1 and (F) for Specimen 2 was captured just before fracture (where damage depth represents a 2D projection of 3D damage into the page), with white outlines containing the crack tip at the specific loading state, and red outlines containing the initial crack tip prior to damage initiation (the crack progressed from left to right). The red circles in (C) and (F) represent fiber breakage points.

and the idealized crack. While the direction of the stress field helps to show why intralaminar cracking was dominant during damage initiation, the intralaminar crack did not grow towards the bottom left, but grew up towards the top right of the notch tip (Fig. 9A, B, C). This is likely due to the fact that the real crack tip, shown in Fig. 9C, is much more tortuous and curves upward, compared to that which is assumed in the homogenized solution. This behavior shows that the exact geometry of the crack plays a crucial role in the directionality of damage initiation, and must be accounted for in the development of accurate damage predictions. As for fiber breakage, it can be seen in Fig. 9C that many of the fiber breakage events occurred at the crack flanks (behind the crack tip) in an apparently stochastic manner, since they did not align with the high stress regions. This apparent stochastic fiber breakage behavior, which was also seen in Figs. 5 and 7 as fiber breakage events with no matrix cracking interaction, likely occurred due to defects induced during fabrication, such as small scratches on the fiber surfaces during tape production or lay-up, as suggested by Garcea et al. in the analysis of a $[90/0]_s$ layup [41].

For Specimen 2 ($[+45/-45/+45]_s$), the analytical solution shows a similar mirrored trend, as can be seen in Fig. 9D and E. While the experimental matrix cracking in Fig. 9F matched the direction of the computed stress field, it showed damage events ahead of the crack tip, not related to the high stresses near notch tip. For example, in the top right of Fig. 9F, an intralaminar cracking event and a number of fiber breakage events are observed, even though they are relatively far away from the notch tip and from the high stresses computed analytically. This observed behavior is due to the presence of plies which are oriented such that the fiber direction is opposite of the ply shown in Fig. 9D–F. The opposing ply in this specimen allows for a redistribution of stress, sometimes much further ahead of the crack tip, which cannot be captured in the analytical solution of one ply. While this may appear to cause increased damage further ahead of the notch tip, overall it is the phenomenon which provides ductility and the ability for slow crack growth.

5. Conclusion

There is an increasing need for damage tolerant approaches in the design of new components and the evaluation of aging structures built with composite laminates. This is mainly because the microstructural damage evolution through certain composite laminate material configurations is not well understood. In this study, *in-situ* synchrotron X-ray micro-computed tomography scans were acquired under monotonic loading conditions which enabled direct observations and detailed investigation of the damage initiation and evolution in the presence of a sharp notch tip in compact tension specimens. Specifically, a T650/5320 composite was used to manufacture two compact tension coupons in two different lay-up configurations ($[+45]_6$ and $[+45/-45/+45]_s$). The analysis showed that in the vicinity of the sharp notch tip, damage initiation in both $[+45]_6$ and $[+45/-45/+45]_s$ formed due to intralaminar cracking. Additionally, damage initiation in $[+45/-45/+45]_s$ showed fiber breakage events. Damage propagation in $[+45]_6$ showed rapid growth of intralaminar matrix cracking, with fiber breakage events near the notch tip only appearing just before final fracture. In general, the $[+45]_6$ layup configuration showed no interaction between fiber breakage and matrix cracking.

On the other hand, damage propagation in $[+45/-45/+45]_s$ was in the form of both intralaminar cracking and delamination, with fiber breakage consistently becoming more prevalent as matrix cracking grew. In general for the $[+45/-45/+45]_s$ layup, a relationship was observed between matrix cracking and fiber breakage, where intralaminar matrix cracking led to 66% of the fiber breakage events. Additionally, it was shown that fiber bridging occurred at a site of +45°/−45° delamination, providing evidence that fiber bridging can be an active toughening mechanism even if delamination is aligned with the loading direction (in contrast to a classic Mode I DCB fracture test). The stress fields assessed via a homogenized analytical solution proved useful in representing the trends followed by the observed damage in both specimens, where it was shown that the majority of fiber breakage events in $[+45]_6$ were stochastic and occurred away from the highly stressed regions. The limitations of the homogenized analytical stress solution reinforced the need to include the exact morphology of the damage source in future fracture predictions. Overall, the results shed light on the exact micromechanical interactions at the sharp notch tip of $[+45]_6$ and $[+45/-45/+45]_s$ T650/5320 compact tension specimens. This study represents an important first step towards the adoption of damage tolerant approaches in the engineering design and qualification of carbon fiber reinforced polymer composites. Future work should focus on re-adapting the loading configuration to allow for a compact tension geometry that aligns with ASTM standards as closely as possible. Additionally, next steps include fatigue testing to provide additional critical information for improved predictive capabilities and the eventual development of a slow crack growth criteria.

CRediT authorship contribution statement

Alejandra M. Ortiz-Morales: Formal analysis, Data curation, Validation, Visualization, Writing - original draft. **Imad Hanhan:** Conceptualization, Methodology, Investigation, Data curation, Visualization, Writing - original draft. **Jose Javier Solano:** Investigation, Formal analysis, Visualization, Data curation, Writing - review & editing. **Michael D. Sangid:** Conceptualization, Methodology, Investigation, Supervision, Project administration, Funding acquisition, Writing - review & editing.

Declaration of competing interest

The authors declare that they have no known competing financial interests or personal relationships that could have appeared to influence the work reported in this paper.

Data statement

The authors will make the data available upon request.

Acknowledgments

Support for this work was provided by the National Science Foundation, USA CMMI MoM, Award No. 1662554 (Program Manager Dr. Siddiq Qidwai), and Technical Data Analysis, Inc., USA Sub Contract No. 2111-001-01 (Program Manager Dr. Chance McColl), based on a Navy SBIR with Contract No. N68335-19-C-0546. The authors would like to thank Dr. Nam Phan of NAVAIR for helpful discussions that helped shape this work. The authors would like to acknowledge Dr. Francesco De Carlo from Argonne National Laboratory for providing algorithms that were used during data acquisition, Ronald Agyei from Purdue University for helping acquire the X-ray projections, and Pavel Shevchenko from Argonne National Laboratory for helping during experimental setup. The authors would like to thank Dr. Prabodha Jayathilaka and Dr. Waruna Seneviratne at the National Institute for Aviation Research at Wichita State University for manufacturing the carbon/epoxy laminate coupons, as well as Jennifer Bergeson from Purdue University for designing the clevis grips. This research used resources of the Advanced Photon Source, a U.S. Department of Energy (DOE) Office of Science User Facility operated for the DOE Office of Science by Argonne National Laboratory under Contract No. DE-AC02-06CH11357.

References

[1] Hull D, Shi YB. Damage mechanism characterization in composite damage tolerance investigations. Compos Struct 1993;23(2):99–120. http://dx.doi.org/10.1016/0263-8223(93)90015-I.
[2] Wang SS. Fracture mechanics for Delamination Problems in Composite Materials. Stud Appl Mech 1984;17(May):369–83.
[3] Murri GB, Guynn EG. Analysis of delamination growth from matrix cracks in laminates subjected to bending loads. In: Composite materials: Testing and design (Eighth Conference). ASTM International; 1988, p. 1–38.
[4] Czabaj MW, Ratcliffe JG. Comparison of intralaminar and interlaminar mode i fracture toughnesses of a unidirectional IM7/8552 carbon/epoxy composite. Compos Sci Technol 2013;89:15–23. http://dx.doi.org/10.1016/j.compscitech.2013.09.008.
[5] Altus E, Ishai O. Transverse cracking and delamination interaction in the failure process of composite laminates. Compos Sci Technol 1986;26(1):59–77. http://dx.doi.org/10.1016/0266-3538(86)90056-4.
[6] Schilling PJ, Karedla BPR, Tatiparthi AK, Verges MA, Herrington PD. X-ray computed microtomography of internal damage in fiber reinforced polymer matrix composites. Compos Sci Technol 2005;65(14):2071–8. http://dx.doi.org/10.1016/j.compscitech.2005.05.014.
[7] Aroush DRB, Maire E, Gauthier C, Youssef S, Cloetens P, Wagner HD. A study of fracture of unidirectional composites using in situ high-resolution synchrotron X-ray microtomography. Compos Sci Technol 2006;66(10):1348–53. http://dx.doi.org/10.1016/j.compscitech.2005.09.010.
[8] Garrett KW, Bailey JE. Multiple transverse fracture in 90° cross-ply laminates of a glass fibre-reinforced polyester. J Mater Sci 1977;12(1):157–68. http://dx.doi.org/10.1007/BF00738481.
[9] Hallett SR, Green BG, Jiang WG, Wisnom MR. An experimental and numerical investigation into the damage mechanisms in notched composites. Composites A 2009;40(5):613–24. http://dx.doi.org/10.1016/j.compositesa.2009.02.021.
[10] Chang F-K, Chang K-Y. A progressive damage model for Laminated composites containing stress concentrations. J Compos Mater 1987;21(9):834–55. http://dx.doi.org/10.1177/002199838702100904, URL http://journals.sagepub.com/doi/10.1177/002199838702100904.
[11] Chang FK, Scott RA, Springer GS. Failure of composite Laminates containing Pin Loaded Holes—Method of solution. J Compos Mater 1984;18(3):255–78. http://dx.doi.org/10.1177/002199838401800305.
[12] Soden PD, Hinton MJ, Kaddour AS. A comparison of the predictive capabilities of current failure theories for composite laminates. Compos Sci Technol 1998;58(7):1225–54. http://dx.doi.org/10.1016/S0266-3538(98)00077-3.
[13] Molent L, Forrester C. The lead crack concept applied to defect growth in aircraft composite structures. Compos Struct 2017;166:22–6. http://dx.doi.org/10.1016/j.compstruct.2016.12.076.
[14] Ttsai S. Composite materials: Testing and design. In: Fifth conference on composite materials: Testing and design. New Orleans, La: American Society for Testing and Materials; 1979, p. 1–689, URL https://www.astm.org/DIGITAL_LIBRARY/STP/SOURCE_PAGES.OLD/STP674_foreword.pdf.
[15] Barbero EJ, Abdelal GF, Caceres A. A micromechanics approach for damage modeling of polymer matrix composites. Compos Struct 2005;67(4):427–36. http://dx.doi.org/10.1016/j.compstruct.2004.02.001.
[16] Federal Aviation Authority. Airworthiness advisory circular No: 20-107B. Tech. rep., U.S. Department of Transportation; 2009, URL https://www.faa.gov/documentLibrary/media/Advisory_Circular/AC20-107B.pdf.
[17] Jones R, Kinloch AJ, Hu W. Cyclic-fatigue crack growth in composite and adhesively-bonded structures: The FAA slow crack growth approach to certification and the problem of similitude. Int J Fatigue 2016;88:10–8. http://dx.doi.org/10.1016/j.ijfatigue.2016.03.008.
[18] Garcea SC, Wang Y, Withers PJ. X-ray computed tomography of polymer composites. Compos Sci Technol 2018;156:305–19. http://dx.doi.org/10.1016/j.compscitech.2017.10.023.
[19] Maire E, Withers PJ. Quantitative X-ray tomography. Int Mater Rev 2014;59(1):1–43. http://dx.doi.org/10.1179/1743280413y.0000000023.
[20] Wright P, Moffat A, Sinclair I, Spearing SM. High resolution tomographic imaging and modelling of notch tip damage in a laminated composite. Compos Sci Technol 2010;70(10):1444–52. http://dx.doi.org/10.1016/j.compscitech.2010.04.012.
[21] Garcea SC, Mavrogordato MN, Scott AE, Sinclair I, Spearing SM. Synchrotron computed tomography of fatigue micromechanisms in CFRP. In: Proc. of the 19th international conference on composite materials. 2013. p. 4802–10.
[22] Moffat A, Wright P, Helfen L, Baumbach T, Johnson G, Spearing S, Sinclair I. In situ synchrotron computed laminography of damage in carbon fibre–epoxy [90/0]s laminates. Scr Mater 2010;62(2):97–100. http://dx.doi.org/10.1016/j.scriptamat.2009.09.027, URL https://www.sciencedirect.com/science/article/pii/S1359646209005983 https://linkinghub.elsevier.com/retrieve/pii/S1359646209005983.
[23] Wu SC, Xiao TQ, Withers PJ. The imaging of failure in structural materials by synchrotron radiation X-ray microtomography. Eng Fract Mech 2017;182:127–56. http://dx.doi.org/10.1016/j.engfracmech.2017.07.027.
[24] Wang Y, Mikkelsen LP, Pyka G, Withers PJ. Time-lapse helical X-ray computed tomography (CT) study of tensile fatigue damage formation in composites for wind turbine blades. Materials 2018;11(11). http://dx.doi.org/10.3390/ma11112340.
[25] Wright P, Fu X, Sinclair I, Spearing SM. Ultra high resolution computed tomography of damage in notched carbon fiber-epoxy composites. J Compos Mater 2008;42(19):1993–2002. http://dx.doi.org/10.1177/0021998308092211.

[26] Scott AE, Mavrogordato M, Wright P, Sinclair I, Spearing SM. In situ fibre fracture measurement in carbon-epoxy laminates using high resolution computed tomography. Compos Sci Technol 2011;71(12):1471–7. http://dx.doi.org/10.1016/j.compscitech.2011.06.004.
[27] Prewo KM. The effect of ply lay-up sequence on the fracture toughness of boron aluminum. J Compos Mater 1978;12(1):40–52.
[28] Laffan MJ, Pinho ST, Robinson P, McMillan AJ. Translaminar fracture toughness testing of composites: A review. Polym Test 2012;31(3):481–9.
[29] Solvay. Thornel T650. 2020, URL https://www.solvay.com/en/product/thornel-t650.
[30] Man M. Solvay cytec cycom 5320-1 T650 unitape qualification material property data report. Tech. rep., National Center for Advanced Materials Performance; 2017, URL https://www.wichita.edu/research/NIAR/Research/cytec-5320-1/T650-Unitape-2.pdf.
[31] Landes J, Bhambri S, Lee K. Fracture toughness testing of polymers using small compact specimens and normalization. J Test Eval 2003;31(2):126–32. http://dx.doi.org/10.1520/JTE12409J, URL https://www.astm.org/DIGITAL_LIBRARY/JOURNALS/TESTEVAL/PAGES/JTE12409J.htm.
[32] Gürsoy D, De Carlo F, Xiao X, Jacobsen C. TomoPy: A framework for the analysis of synchrotron tomographic data. J Synchrotron Radiat 2014;21(5):1188–93. http://dx.doi.org/10.1107/S1600577514013939.
[33] Pelt DM, Gürsoy D, Palenstijn WJ, Sijbers J, De Carlo F, Batenburg KJ. Integration of TomoPy and the ASTRA toolbox for advanced processing and reconstruction of tomographic synchrotron data. J Synchrotron Radiat 2016;23(3):842–9. http://dx.doi.org/10.1107/S1600577516005658.
[34] Abràmoff MD, Magalhães PJ, Ram SJ. Image processing with ImageJ. Biophotonics Int 2004;11(7):36–42.
[35] Hanhan I, Sangid MD. ModLayer: A MATLAB GUI drawing segmentation tool for visualizing and classifying 3D data. Integr Mater Manuf Innov 2019;8(0123456789):468–75. http://dx.doi.org/10.1007/s40192-019-00160-5, URL https://doi.org/10.1007/s40192-019-00160-5 http://link.springer.com/10.1007/s40192-019-00160-5.
[36] Ahrens J, Geveci B, Law C. Paraview: An end-user tool for large data visualization. Vis Handb 2005;717.
[37] Sih GC, Paris PC, Irwin GR. On cracks in rectilinearly anisotropic bodies. Int J Fract Mech 1965;1(3):189–203. http://dx.doi.org/10.1007/BF00186854.
[38] Khan R. Fiber bridging in composite laminates: A literature review. Compos Struct 2019;229:111418.
[39] Spearing SM, Evans AG. The role of fiber bridging in the delamination resistance of fiber-reinforced composites. Acta Metall Mater 1992;40(9):2191–9.
[40] Gong Y, Zhao L, Zhang J, Wang Y, Hu N. Delamination propagation criterion including the effect of fiber bridging for mixed-mode I/II delamination in CFRP multidirectional laminates. Compos Sci Technol 2017;151:302–9.
[41] Garcea SC, Sinclair I, Spearing SM, Withers PJ. Mapping fibre failure in situ in carbon fibre reinforced polymers by fast synchrotron X-ray computed tomography. Compos Sci Technol 2017;149:81–9. http://dx.doi.org/10.1016/j.compscitech.2017.06.006.